



Aki and Lee (1976) and Dziewonski et al. (1977), tomographic images have provided crucial information to the understanding of plate tectonics, volcanism and geodynamics (e.g. Romanowicz, 1991; Liu and Gu, 2012; Zhao, 2012). Seismic tomography itself also went through significant development over the last three decades, including advances in both methodology and data usage.

In the first two decades of its history, seismic tomography is mainly based on the ray theory which assumes that seismic traveltime is determined by the structure along the infinitely thin ray path only. However, because of scattering, wave front healing and other finite-frequency effects, seismic measurements (such as traveltime and amplitude), especially those made on broadband recordings, are sensitive to three-dimensional (3-D) structures off the ray path (e.g. Marquering et al., 1999; Dahlen et al., 2000; Tape et al., 2007). Ray theory is actually only valid when the scale length of the variation of material properties is much larger than the seismic wavelength (Rawlinson et al., 2010). To take into account the influence of off-ray structures, finite-frequency tomography methods in which 2-D or 3-D traveltime and amplitude sensitivity kernels are constructed, including those based on the paraxial approximation and dynamic ray tracing (e.g. Marquering et al., 1999; Dahlen et al., 2000; Tian et al., 2007; Tong et al., 2011) and those based on the normal mode theory (e.g. Zhao et al., 2000; Zhao and Jordan, 2006; To and Romanowicz, 2009). Tomographic models with improved resolutions were reported by recent finite-frequency tomographic studies (e.g. Montelli et al., 2004; Hung et al., 2004, 2011; Gautier et al., 2008), although comparison to ray-based tomography remains controversial (de Hoop and van der Hilst, 2005a; Dahlen and Nolet, 2005; de Hoop and van der Hilst, 2005b). The underlying problem of the finite-frequency tomography based on paraxial approximation and dynamic ray tracing is that its kernel computation still relies on the ray theory, although it was devised to account for non-geometrical finite-frequency phenomena. In the last decade or so, rapid advances in high-performance computing and forward modelling techniques make it feasible to solve the seismic wave equations in realistic Earth models by full numerical methods (e.g. Komatitsch and Tromp, 2002a, b; Komatitsch et al., 2004; Operto

2525

et al., 2007). This opens the way to compute sensitivity kernels based on numerical simulation of the full seismic wavefield, avoiding the use of approximate theories (e.g. Liu and Tromp, 2006, 2008; Fichtner et al., 2009). It also made the conceptual wave-equation based seismic inversion methods such as the one presented by Tarantola (1984) feasible in realistic applications (Tape et al., 2009; Fichtner and Trampert, 2011; Zhu et al., 2012). To our best knowledge, adjoint tomography (Tromp et al., 2005; Fichtner et al., 2006), scattering integral methods (L. Zhao et al., 2005; Chen et al., 2007b), and full waveform inversion (FWI) in the frequency domain (Pratt and Shipp, 1999; Operto et al., 2006) are among the most popular tomographic techniques based upon solving full wave equations. FWI in frequency domain has been mainly used in exploration problems (e.g. Virieux and Operto, 2009; Lee et al., 2010) for relative small and regular simulation domains. Adjoint tomography and scattering integral tomography are closely related to each other, and a detailed comparison between adjoint tomography and scattering integral tomography can be found in Chen et al. (2007a). For brevity, we restrict our following discussions to adjoint tomography (Liu and Gu, 2012).

Adjoint tomography is currently one of the most popular and promising tomographic methods for resolving strongly varying structures. It takes advantages of full 3-D numerical simulations in forward modelling and sensitivity kernel calculation, often iteratively improves models through optimization techniques (Tromp et al., 2005; Tape et al., 2007). The use of full numerical simulations allows for the freedom of choosing either 1-D or 3-D reference models and accurate calculations of seismograms (Tong et al., 2014a) and sensitivity kernels for complex models (Liu and Tromp, 2006, 2008). Using this approach, Tape et al. (2009, 2010) obtained a 3-D velocity model of the southern California crust that captures strong local heterogeneity up to  $\pm 30\%$ . Similarly, Zhu et al. (2012) generated a tomographic model of the European upper mantle based on adjoint tomography that reveals nice correlations between structural features and regional tectonics and dynamics. Similarly, Rickers et al. (2013) presented a 3-D  $S$  wave velocity model of the North Atlantic region, revealing structural features in unprecedented detail down to the depth of 1300 km. These successful applications reveal

2526

the promising future of next generation seismic tomographic models based on full numerical simulations. However, the expensive computation cost associated with adjoint-type of wave-equation-based tomographic methods, especially for 3-D problems, is still a major stumbling block to its wider applications. For example, for a moderate number of three-component seismograms, 0.8 million and 2.3 million central processing unit hours were used to generate the tomographic models of the southern California crust and the European upper mantle, respectively (Tape et al., 2009; Zhu et al., 2012). The severity of the cost issue may be remedied when simulations are ported to the Graphic Processing Unit (GPU) hardwares (e.g. Komatitsch et al., 2010; Michéa and Komatitsch, 2010). However, ray-based tomographic methods remains the most popular and accessible techniques in mapping the heterogeneous structures of the Earth's interior (e.g. Li et al., 2008; Hung et al., 2011; Tong et al., 2012; Zhao et al., 2012).

As mentioned above, full 3-D numerical simulations in forward modelling and sensitivity kernel calculations guarantee the accuracy of synthetic seismograms and sensitivity kernels for 3-D complex models. But they also make adjoint tomography computationally demanding and even unaffordable. To strike a balance between the computational efficiency and accuracy of full wave-equation based tomographic methods, we propose to conduct the forward modelling and sensitivity kernel calculation in the 2-D source-receiver vertical plane by a high-order finite-difference scheme. As we will show, if only traveltimes measurements are considered, this 2-D approximation offers acceptable accuracy. Meanwhile, by numerically solving 2-D wave equations, finite-frequency effects such as wavefront healing are naturally taken into account, and the accuracy of sensitivity kernels in complex heterogeneous models is also improved. Although forward modellings are restricted to 2-D planes, we still plan to invert for 3-D tomographic models on a 3-D inversion grid. The 2-D forwarding modelling and the 3-D tomographic inversion are linked by expressing the model parameters (such as velocity perturbation) at each 2-D forward modelling grid node as a linear interpolation of the model parameters at its surrounding 3-D inversion grid nodes. We name the resultant 2-D-3-D tomographic method as wave-equation based traveltimes seismic tomography

2527

(WETST). Comparing with the 3-D-3-D adjoint tomography based on the spectral element method (Tromp et al., 2005; Fichtner et al., 2006), this 2-D-3-D WETST based upon a 2-D finite-difference scheme is generally more computationally affordable. This also entails that WETST can be applied to tomographic inversions involving significant amount of data based on even moderate computational resources.

Arrival time picking is another important issue for traveltimes seismic tomography. Since the early era of ray-based seismic tomography, researchers have mainly relied on manually picked arrival times to map subsurface structures (e.g. Aki and Lee, 1976; Zhao et al., 1992). Arrival times are usually picked within time windows centred at the predicted traveltimes (Kennett and Engdahl, 1991; Maggi et al., 2009). In recent years, increasingly number of deployed broadband seismic arrays have resulted in the proliferation of seismic data. To increase efficiency and reduce the amount of manual labour and human errors in seismic data processing, fast and automatic traveltimes picking algorithms with high accuracy are highly demanded to process vast amount of seismic recordings. Indeed, various techniques have been presented for automatic/semi-automatic detecting and picking the arrivals of different seismic phases, and the most widely used of which is the short-term-average (STA) to long-term-average (LTA) ratio method and its variations (e.g. Coppens, 1985; Baer and Kradolfer, 1987; Saari, 1991; Earle and Shearer, 1994; Han et al., 2010). Zhang et al. (2003) developed an automatic  $P$  wave arrival detection and picking algorithm based on the wavelet transform and Akaike information criteria. Cross-correlation method is another routinely used technique to obtain the traveltimes anomalies of broadband pulses, which is specially favoured by finite-frequency tomographic applications (e.g. Luo and Schuster, 1991; Dahlen et al., 2000; Tape et al., 2007). However, the quality of picked arrivals by these methods may vary in accuracy for datasets of different signal-to-noise ratio (SNR), and often only arrivals on low-noise seismograms can be effectively picked (Akram, 2011). Specifically, the validity of the correlation-based methods requires that the synthetic seismograms be reasonably similar to the observed seismograms. Less restrictive automatic arrival picking algorithms need to be further developed. In this study, we pro-

2528























phases in the reference model. As shown in Fig. 5a and b, the geometrical ray paths of both phases are partially within the low velocity zone, and therefore it is reasonable to have delayed S and SmS arrivals in the “true” model. For the sSmS phase, its geometrical ray path does not pass through the low velocity zone but its first Fresnel zone partially coincides with the low velocity anomaly (Fig. 4c). Due to the influence of the low velocity zone, the arrival time of sSmS is delayed by 0.0025 s obtained through cross-correlation calculation. The Fréchet kernels for S, SmS and sSmS are shown in Fig. 5a–c, which closely follows their corresponding geometry ray paths (indicated by dashed lines). The positive Fréchet kernel values in the first Fresnel zones indicate that a reduction of velocity within these regions will result in the reduction of objective function  $\chi$ . Figures 4b and 5d–f are for the case when seismic waves travel through a high velocity region in the “true” model and seismograms are recorded at the station  $x = 86.0$  km. Negative Fréchet kernel values in the first Fresnel zones suggest that an increase of velocity in this region of the reference model can reduce the objective function  $\chi$ .

The Fréchet kernels displayed in Fig. 5a–f are associated with a particular seismic phase at one seismic station, i.e. the individual kernels. Of course one seismic record does not well constrain the subsurface heterogeneous structure. With the 51 stations on the surface, we could compute the Fréchet kernel for one seismic phase defined at all seismic stations, shown in Fig. 5g–i. These kernels are actually the sum of individual S, SmS and sSmS kernels computed at each station. Due to the increased data coverage and the constructive effect, both the low and high velocity areas are sampled by the bulk part of the kernels. The values of these three kernels are positive within the low velocity zone and negative within the high velocity area, which indicates that updating the velocity model in the opposite direction  $-\partial\chi(\mathbf{X})/\partial\mathbf{X}$  would reduce the objective function  $\chi$ . We could further define the objective function  $\chi$  as the sum of S, SmS and sSmS phases at all seismic stations. The corresponding Fréchet kernel is shown in Fig. 6, which is the sum of the kernels in Fig. 5g–i. It can be observed that kernel values at the anomalous regions are not prominent in Fig. 5g–i, but are dominant

2549

in Fig. 6. This suggests that we may simultaneously use different seismic phase data to highlight anomalous structures in future study. For demonstration purpose, we only worked with one event in this part. To increase the illumination, more seismic events should be included. Once the Fréchet kernels for all events and phases are computed, the LSQR solver or the non-linear conjugate-gradient method can be used to iteratively improve the velocity model.

## 7 Discussion and conclusions

Wave-equation based traveltimes seismic tomography (WETST) involves 2-D forward modelling and 3-D tomographic inversion. Considering adjoint tomography based on 3-D spectral-element method as an approach for “3-D-3-D” seismic tomography (e.g. Tromp et al., 2005; Tape et al., 2009; Zhu et al., 2012), WETST can be viewed as a “2-D-3-D” adjoint tomography technique. From the computation point of view, 2-D forward modelling with a high-order central difference scheme is computationally efficient and can be conducted on most single PCs. This makes it possible to handle large seismic data sets with WETST. Actually, increasing data amount and data coverage is the best way to improve the resolution of tomographic results, and sometimes may compensate for the approximations in the tomography technique itself. For example, it is well known that one main drawback of ray theory is that it does not consider the influence of off-ray structures (Dahlen et al., 2000), but a good data set with a dense and even distribution of ray paths can greatly improve the resolution of ray tomography (Tong et al., 2011). A similar problem for the 2-D approximation in WETST is its ignorance of the off-plane influence on seismic arrivals. To what extent this approximation is valid and how it affects the final inversion results should be further investigated. But taking advantage of the computational efficiency of 2-D forward modelling, we may be able to reduce the effect of the 2-D approximation by increased data coverage in real applications.

WETST only uses traveltimes information for two main reasons. First, traveltimes is quasi-linear with respect to variations in the velocity structures, which greatly assists

2550

the convergence of gradient-based inversion methods as presented in Sect. 5. Second, compared with fitting waveforms, it is much easier to predict the arrival times of particular phases on synthetic seismograms computed through 2-D forward modelling. The envelop energy method or the combined ray and cross-correlation method presented in this study can be easily implemented to pick the arrival times on synthetic seismograms.

If 3-D finite-frequency effects need to be taken into account and full waveform fitting is required, we suggest the use of “3-D-3-D” tomographic techniques such as adjoint tomography based on spectral-element method (Tromp et al., 2005; Fichtner et al., 2006). In this case, WETST may be used to construct the starting models for “3-D-3-D” seismic tomography. The hybrid approach could help reduce the total computational costs and speed up the convergence rate of the inverse algorithm as a “closer” initial model is used. Considering that ray-based seismic tomography methods are still the most prevalent tomographic methods and WETST has the advantage of more accurately computed sensitivity kernels, WETST may be a potentially useful compromise for 3-D tomographic inversions before the wider application of “3-D-3-D” seismic tomography in the near future.

Forward modelling in WETST discussed in this paper is based on solving a 2-D acoustic wave equation in the Cartesian coordinates. If the source and the receiver are far away apart and the curvature of the Earth cannot be neglected, the acoustic wave equation in Cartesian coordinates needs to be transformed into geographical coordinates, which may be necessary for the use of teleseismic data. Currently, WETST cannot use converted seismic phases such as  $P$ - $S$  or simultaneously determine the  $P$  wave and  $S$  wave velocity structures in tomographic inversions. But these two goals can be achieved by replacing the 2-D acoustic wave equation with the 2-D elastic wave equation. Additionally, a regular grid with variable grid intervals is suggested to represent the final tomographic results in this paper. To automatically adapt the inversion grid to the data distribution, adaptive mesh using Delaunay triangles and Voronoi polyhedra can be alternatively adopted (e.g. Sambridge and Rawlinson, 2005; Zhang and

2551

Thurber, 2005; Rawlinson et al., 2010). Source inversion and discontinuity (such as the depth of Moho) determination may also be considered in the future (e.g. Liu and Tromp, 2008; Tong et al., 2014a).

In addition, WETST can include not only direct first arrivals ( $P$  wave and  $S$  wave) but also later reflected (e.g.  $PmP$ ,  $SmS$ ,  $pPmP$ ,  $sSmS$ ) and refracted ( $Pn$ ,  $Sn$ ) phases as the ray-based tomographic methods do (e.g. D. Zhao et al., 1992, 2005; Xia et al., 2007). Different seismic phases have different travelling paths and are influenced by structural anomalies differently. The combining use of various seismic phases can increase the illumination of the subsurface structures (Figs. 5 and 6). Since WETST conducts forward modelling in 2-D vertical planes with an efficient high-order central difference scheme, it is possible to include a large set of seismic data in tomographic inversion. Two different inversion algorithms, LSQR solver and the non-linear conjugate-gradient method, can be used to find the optimal tomographic results with efficiency. In a companion paper, we will use WETST to explore the heterogeneous structures beneath the 1992 Landers earthquake ( $M_w$  7.3) area.

## 5 Appendix A: High-order central difference method

Yang et al. (2012) developed a finite-difference scheme, nearly-analytic central difference (NACD) method, to solve the 2-D acoustic wave equation. The NACD method has fourth-order accuracies in both space and time, and it uses only three grid nodes in each spatial direction. This method shows a good performance in suppressing numerical dispersions. The essence of the NACD method is to use displacement and its spatial gradient to approximate second and higher order spatial derivatives of the displacement. To achieve this goal, the displacement gradient field is obtained by numerically solving some derived acoustic wave equations (Yang et al., 2012). For simplicity, we use a simplified version of the NACD method to simulate 2-D acoustic wave propagation. In this approach, the value of the spatial gradient along one axis at a particular node is interpolated by the displacement values at its neighbouring grid nodes.

2552









- Tape, C., Liu, Q., Maggi, A., and Tromp, J.: Seismic tomography of the southern California crust based on spectral-element and adjoint methods, *Geophys. J. Int.*, 180, 433–462, 2010.
- Tarantola, A.: Inversion of seismic reflection data in the acoustic approximation, *Geophysics*, 49, 1259–1266, 1984.
- 5 Tarantola, A.: *Inverse Problem Theory and Methods for Model Parameter Estimation*, 1st edn., Society for Industrial and Applied Mathematics, Philadelphia, 2005.
- Thurber, C. H.: Earthquake locations and three-dimensional crustal structure in the Coyote Lake area, central California, *J. Geophys. Res.*, 88, 8226–8236, 1983.
- Tian, Y., Montelli, R., Nolet, G., and Dahlen, F.: Computing travel-time and amplitude sensitivity kernels in finite-frequency tomography, *J. Comput. Phys.*, 226, 2271–2288, 2007.
- 10 To, A. and Romanowicz, B.: Finite frequency effects on global S diffracted traveltimes, *Geophys. J. Int.*, 179, 1645–1657, 2009.
- Tong, P., Zhao, D., and Yang, D.: Tomography of the 1995 Kobe earthquake area: comparison of finite-frequency and ray approaches, *Geophys. J. Int.*, 187, 278–302, 2011.
- 15 Tong, P., Zhao, D., and Yang, D.: Tomography of the 2011 Iwaki earthquake (M 7.0) and Fukushima nuclear power plant area, *Solid Earth*, 3, 43–51, doi:10.5194/se-3-43-2012, 2012.
- Tong, P., Chen, C.-W., Komatitsch, D., Basini, P., and Liu, Q.: High-resolution seismic array imaging based on an SEM-FK hybrid method, *Geophys. J. Int.*, 197, 369–395, 2014a.
- 20 Tong, P., Zhao, D., Yang, D., Yang, X., Chen, J., and Liu, Q.: Wave-equation based traveltimes seismic tomography – Part 2: Application to the 1992 Landers earthquake ( $M_w$  7.3) area, *Solid Earth Discuss.*, 5, 2567–2613, doi:10.5194/sed-5-2567-2014, 2014b.
- Tromp, J., Tape, C., and Liu, Q.: Seismic tomography, adjoint methods, time reversal and banana-doughnut kernels, *Geophys. J. Int.*, 160, 195–216, 2005.
- 25 Virieux, J.: SH-wave propagation in heterogeneous media: velocity-stress finite difference method, *Geophysics*, 49, 1933–1942, 1984.
- Virieux, J. and Operto, S.: An overview of full-waveform inversion in exploration geophysics, *Geophysics*, 74, WCC1–WCC26, 2009.
- Wessel, P. and Smith, W. H. F.: Free software helps map and display data, *EOS T. Am. Geophys. Un.*, 72, 441–448, 1991.
- 30 Wong, J., Han, L., Bancroft, J., and Stewart, R.: Automatic time-picking of first arrivals on noisy microseismic data, *CSEG*, 2009.

2559

- Xia, S., Zhao, D., Qiu, X., Nakajima, J., Matsuzawa, T., and Hasegawa, A.: Mapping the crustal structure under active volcanoes in central Tohoku, Japan using P and PmP data, *Geophys. Res. Lett.*, 34, L10309, doi:10.1029/2007GL030026, 2007.
- 890 Yang, D., Tong, P., and Deng, X.: A central difference method with low numerical dispersion for solving the scalar wave equation, *Geophys. Prospect.*, 60, 885–905, 2012.
- Zhang, H. and Thurber, C.: Adaptive-mesh seismic tomography based on tetrahedral and Voronoi diagrams: application to Parkfield, California, *J. Geophys. Res.*, 110, B04303, doi:10.1029/2004JB003186, 2005.
- 895 Zhang, H., Thurber, C., and Rowe, C.: Automatic P Wave arrival detection and picking with multiscale wavelet analysis for single-component recordings, *B. Seismol. Soc. Am.*, 93, 1904–1912, 2003.
- Zhao, D.: Multiscale seismic tomography and mantle dynamics, *Gondwana Res.*, 15, 297–323, 900 2009.
- Zhao, D.: Tomography and dynamics of Western-Pacific subduction zones, *Monogr. Environ. Earth Planets*, 1, 1–70, 2012.
- Zhao, D., Hasegawa, A., and Horiuchi, S.: Tomographic imaging of P and S wave velocity structure beneath northeastern Japan, *J. Geophys. Res.*, 97, 19909–19928, 1992.
- 905 Zhao, D., Todo, S., and Lei, J.: Local earthquake reflection tomography of the Landers aftershock area, *Earth. Planet. Sc. Lett.*, 235, 623–631, 2005.
- Zhao, D., Yanada, T., Hasegawa, A., Umino, N., and Wei, W.: Imaging the subducting slabs and mantle upwelling under the Japan Islands, *Geophys. J. Int.*, 190, 816–828, 2012.
- Zhao, L. and Jordan, T. H.: Structural sensitivities of finite-frequency seismic waves: a full-wave approach, *Geophys. J. Int.*, 165, 981–990, 2006.
- 910 Zhao, L., Jordan, T. H., and Chapman, C. H.: Three-dimensional Fréchet differential kernels for seismic delay times, *Geophys. J. Int.*, 141, 558–576, 2000.
- Zhao, L., Jordan, T. H., Olsen, K. B., and Chen, P.: Fréchet kernels for imaging regional earth structure based on three-dimensional reference models, *B. Seismol. Soc. Am.*, 95, 2066–915 2080, 2005.
- Zhu, H., Bozdog, E., Peter, D., and Tromp, J.: Structure of the European upper mantle revealed by adjoint tomography, *Nat. Geosci.*, 5, 493–498, 2012.

2560

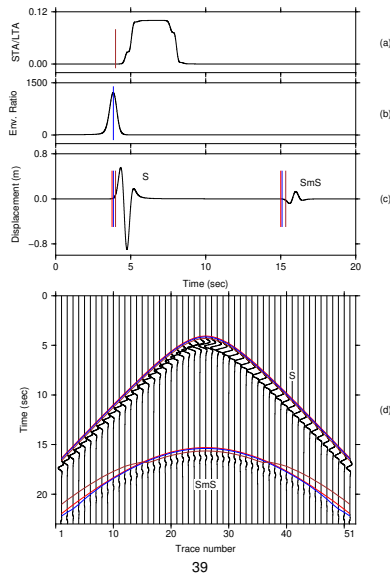


**Figure 1.** *S* arrival time-picking using (a) the STA/LTA method and (b) the envelop energy ratio (EER) method for the synthetic seismogram in (c), which is the seismogram for trace number 26 in (d). (d) Displays synthetic seismograms recorded by 51 stations with an equal spacing of 2 km at the surface, which are generated by an earthquake at the depth 12.0 km directly below the 26th station. The computational domain is a crust over mantle model. The crust has a thickness of 30.0 km and is homogeneous with the *S* wave velocity  $3.2\text{ km s}^{-1}$  in the crust and  $4.5\text{ km s}^{-1}$  in the mantle. In (c) and (d), the arrival times of *S* and Sm*S* phases determined based on the STA/LTA and EER methods are labelled with brown and blue lines, respectively. The theoretical arrivals are marked by red lines.

2561

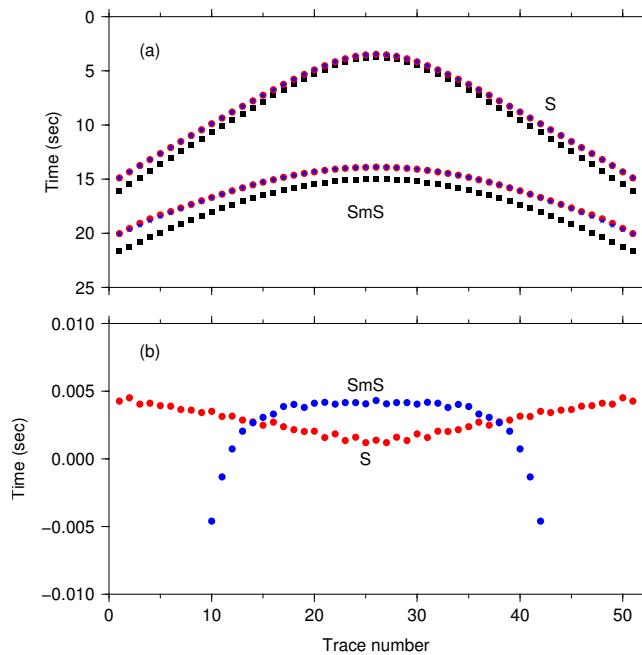


**Figure 2.** (a) *S* and Sm*S* arrival times on seismograms computed in two models  $m_0$  and  $m_1$ . Numerical computation in  $m_0$  is the same as the example shown in Fig. 1. *S* wave velocity in  $m_1$  has a perturbation of 8% with respect to  $m_0$ . Black squares, red circles, and blue stars are corresponding to theoretical arrival times in  $m_0$ , theoretical arrival times in  $m_1$ , and arrival times computed by using the combined ray and cross-correlation method, respectively. (b) Errors of *S* (red circles) and Sm*S* (blue circles) arrival times determined by using the combined ray and cross-correlation method.

2562

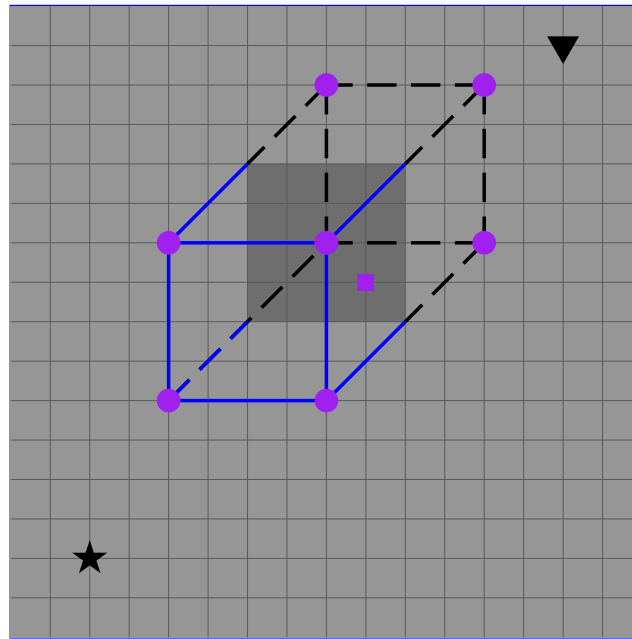


**Figure 3.** Linear interpolation of the material properties on one forward modelling grid node (purple square) with material properties on its eight surrounding inversion grid nodes (purple circles). Forward modelling grid is a regular 2-D mesh with fixed grid intervals (formed by grey lines), and inversion grid is a 3-D regular mesh with variable grid intervals. Black star and black inverse triangle denote the locations of the earthquake and seismic station in the 2-D vertical plane, respectively.

2563

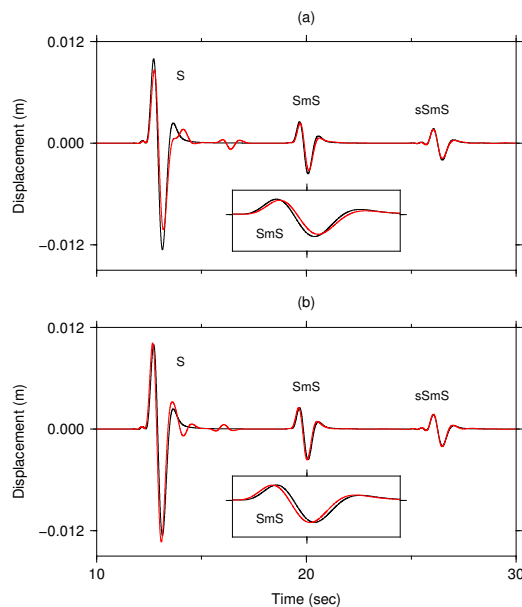


**Figure 4.** Seismograms recorded by the stations located at **(a)**  $x = 14$  km and **(b)**  $x = 86$  km on the surface. Seismograms computed in the reference model are shown as black curves, and those computed in the “true” model are illustrated by red curves. The computational domain is a crust over mantle model with a size of  $100 \text{ km} \times 50 \text{ km}$ . The crust has a thickness of 30 km containing one low and one high velocity zone in the “true” model respect to the reference model (Fig. 5). The earthquake is located at  $x = 50$  km at the depth 12 km.

2564

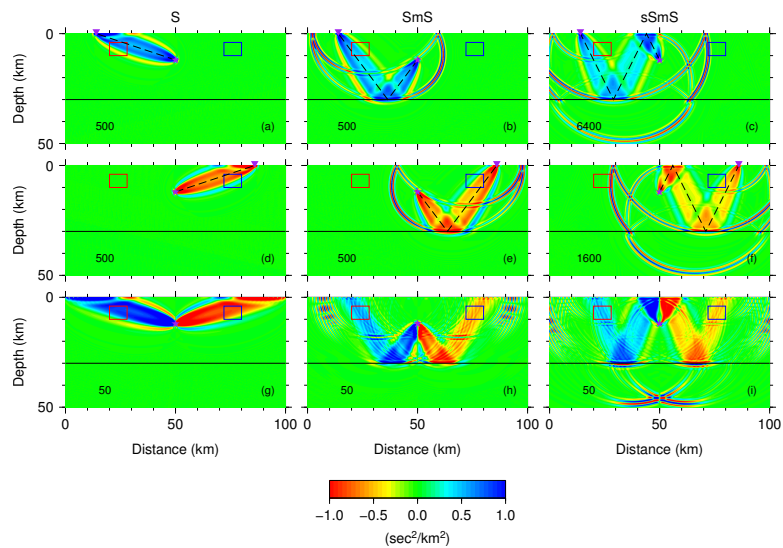


**Figure 5.** Fréchet kernels corresponding to direct S (**a**, **d**, **g**), SmS (**b**, **e**, **h**) and sSmS (**c**, **f**, **i**) phases. (**a**)–(**c**) Are computed only using seismograms recorded at the station  $x = 14$  km. These seismograms are influenced by the low velocity zone in the red box in the “true” model. (**d**)–(**f**) Are only related to seismograms recorded at the station  $x = 86$  km, which are influenced by the high velocity zone in the blue box in the “true” model. (**g**)–(**i**) Are computed for all 51 stations on the surface. To use a uniform colour bar indicated at the bottom for all subfigures, each kernel is amplified by multiplying the number at the left bottom of the corresponding subfigure.

2565

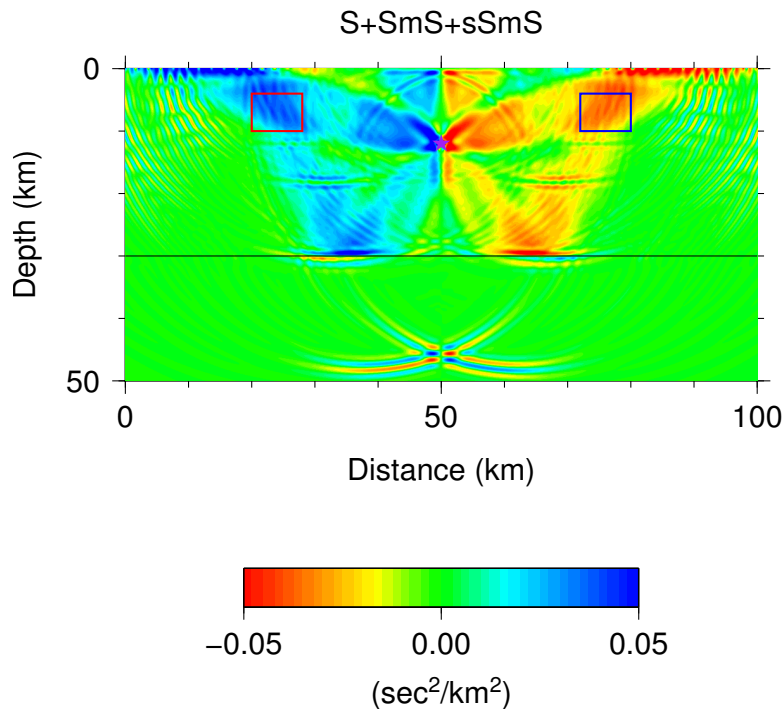


**Figure 6.** Summation of the Fréchet kernels corresponding to the kernels for S, SmS and sSmS phases in Fig. 5g–i.

2566